

# High-Frequency Ultrasound Sensors Using Polymer Microring Resonators

Chung-Yen Chao, Shai Ashkenazi, *Member, IEEE*, Sheng-Wen Huang, *Member, IEEE*,  
Matthew O'Donnell, *Fellow, IEEE*, and L. Jay Guo, *Member, IEEE*

**Abstract**—Polymer microring resonators are demonstrated as high-frequency, ultrasound detectors. An optical microring resonator consists of a ring waveguide closely coupled to a straight bus waveguide, serving as light input and output. Acoustic waves irradiating the ring induce strain, deforming the waveguide dimensions and changing the refractive index of the waveguide via the elasto-optic effect. These effects modify the effective refractive index of the guided mode inside the waveguide. The sharp wavelength dependence of the microring resonance can enhance the optical response to acoustic strain. Such polymer microring resonators are experimentally demonstrated in detecting broadband ultrasound pulses from a 50 MHz transducer. Measured frequency response shows that these devices have potential in high-frequency, ultrasound detection. Design guidelines for polymer microring resonators forming an ultrasound detector array are discussed.

## I. INTRODUCTION

HIGH-RESOLUTION biomedical and industrial applications push ultrasonic imaging technology to its high-frequency limits. High-frequency imaging (above 20 MHz) plays an important role in a variety of areas from basic scientific research, through drug development, to medical diagnosis and nondestructive testing of microelectronics components [1]. For researchers in developmental biology, high-frequency ultrasonic imaging provides noninvasive imaging of mice from very early embryonic stages through neonate and adulthood [2]–[4]. Drug development relies primarily on small animal models [5], [6]. The study of disease progression and therapeutic effects of drugs is greatly enhanced with high-frequency ultrasound imaging. It also is used in medical applications such as intravascular ultrasound (IVUS) [7], diagnosis of skin pathologies [8], ophthalmology [9], [1], and intraurethra catheters for prostate gland imaging [11]. These applications currently rely on piezoelectric transducers.

Piezoelectric technology has significant functional and fabrication challenges as the frequency increases above 20 MHz. At these frequencies, small element size and high-element density are difficult to obtain with piezoelectrics. Transmission of the electrical signal from the ac-

tive piezoelement to the receiver is another source of difficulty due to the relatively large noise level and impedance loading by the transmission line at high frequencies, as well as the large number of electrical conductors needed to address individual sensor elements.

In practical applications, operating frequency is often compromised due to these limitations. State-of-the-art catheter based ultrasonic arrays for IVUS operate at a maximal frequency of 20 MHz [12]. Another approach uses a single element with mechanical scanning. Single-element devices are limited to fixed focusing, which results in nonuniform resolution. They also are limited in their frame rate due to mechanical scanning.

Recently, resonant optical ultrasound transducers (ROUT) have attracted increasing attention. They include microring resonators [13], etalons [14], [15], fiber gratings [16], and dielectric multilayer interference filters [17]. They all rely on the interaction of an optical field confined in a resonance cavity with a transient ultrasonic field. The ultrasonic field can induce strain to modulate the optical properties of the resonance cavity. With a sharp cavity resonance, the optical response to transient strain is amplified.

ROUT sensors can be miniaturized to a size less than 10  $\mu\text{m}$  due to light confinement in the resonant cavity. In contrast to piezoelectric transducers in which size reduction causes excess noise. In optical detection, the noise level is not affected by size reduction. Element miniaturization is an essential requirement for ultrasonic array design at high frequency. For example, phased-array imaging systems working at a center frequency of 50 MHz require  $\lambda/2$  element size and spacing on the order of 15  $\mu\text{m}$ .

In this article, we explore the potential of an optical microring resonator array as a high-frequency ultrasound sensor. In Section II, basic principles and operating theory of a microring ultrasound sensor will be discussed and established. Section III describes the fabrication process of such a detector. Experimental results using the device to detect high-frequency ( $\sim 50$  MHz) ultrasound is illustrated in Section IV. In Section V, we discuss design considerations for a high-frequency, optoacoustic microring array.

## II. PRINCIPLES OF MICRORING ULTRASOUND SENSORS

### A. Microring Resonators

A microring resonator contains a ring waveguide closely coupled to a straight bus waveguide serving as light input

Manuscript received June 22, 2006; accepted December 12, 2006. This work was supported by the NIH under Grant R21 EB004933-01.

C. Y. Chao and L. J. Guo are with the Department of Electrical Engineering and Computer Science at the University of Michigan, Ann Arbor, MI 48109.

S. Ashkenazi, S.-W. Huang, and M. O'Donnell are with the Department of Biomedical Engineering at the University of Michigan, Ann Arbor, MI 48109 (e-mail: shaia@umich.edu).

Digital Object Identifier 10.1109/TUFFC.2007.341

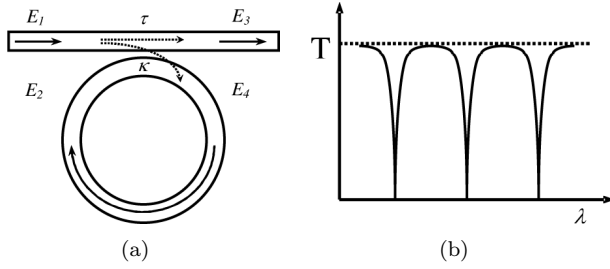


Fig. 1. (a) A microring resonator consists of a ring waveguide closely coupled with a straight waveguide. (b) Typical transmission spectrum of a microring possesses periodic resonant notches.

and output ports, as shown in Fig. 1(a). The ring waveguide forms a resonant optical cavity. The input ( $E_1$ ), output ( $E_3$ ), and circulating fields inside the ring ( $E_2$  and  $E_4$ ) can be described by the following coupled-mode equations:

$$\begin{aligned} E_3 &= \alpha_i(\tau E_1 + j\kappa E_2), \\ E_4 &= \alpha_i(j\kappa E_1 + \tau E_2), \end{aligned} \quad (1)$$

where  $\tau$  and  $\kappa$  are the amplitude transmission and coupling coefficients, respectively, and  $\alpha_i$  is the insertion loss due to the waveguide mode mismatch in the coupling region. By introducing the single-pass amplitude attenuation factor  $a$ , we can express the relation between  $E_2$  and  $E_4$  as:

$$E_2 = ae^{j\phi} E_4, \quad (2)$$

where  $\phi$  is the single-pass phase shift experienced by light traveling inside the microring, equal to  $2\pi n_{\text{eff}}L/\lambda$ . Here  $n_{\text{eff}}$  is the effective refractive index of the mode guided inside the ring waveguide,  $L$  is the circumference of the ring, and  $\lambda$  is the light wavelength. The transmission coefficient, defined as the ratio of the transmitted intensity to the incident intensity, can then be calculated using (1) and (2) to be:

$$T \equiv \frac{I_t}{I_i} = \left| \frac{E_3}{E_1} \right|^2 = \alpha_i^2 \frac{(\tau - \alpha_i a)^2 + 4\tau\alpha_i a \sin^2 \frac{\phi}{2}}{(1 - \tau\alpha_i a)^2 + 4\pi\alpha_i a \sin^2 \frac{\phi}{2}}. \quad (3)$$

Eq. (3) implies a periodic resonant spectrum, as shown in Fig. 1(b), similar to the reflection spectrum in a Fabry-Perot resonant cavity [14]. Resonances occur when the round-trip phase acquired by the guided wave is equal to multiples of  $2\pi$ , i.e.,

$$m\lambda_c = n_{\text{eff}}L, \quad (4)$$

$\lambda_c$  and  $m$  represent the resonant wavelength and resonance order (an integer), respectively. To simplify the calculation, coupling loss is neglected, i.e.,  $\alpha_i = 1$ .

In microring ultrasound sensors, incident acoustic pulses create a stress field, which can slightly deform the waveguide dimension, as illustrated in Fig. 2(a). The change in waveguide cross section directly modifies the effective refraction index of the guided mode. Moreover, the strain simultaneously modifies the refractive indices of the waveguide material and water (surrounding the waveguide) via the elasto-optic effect. Both phenomena influence

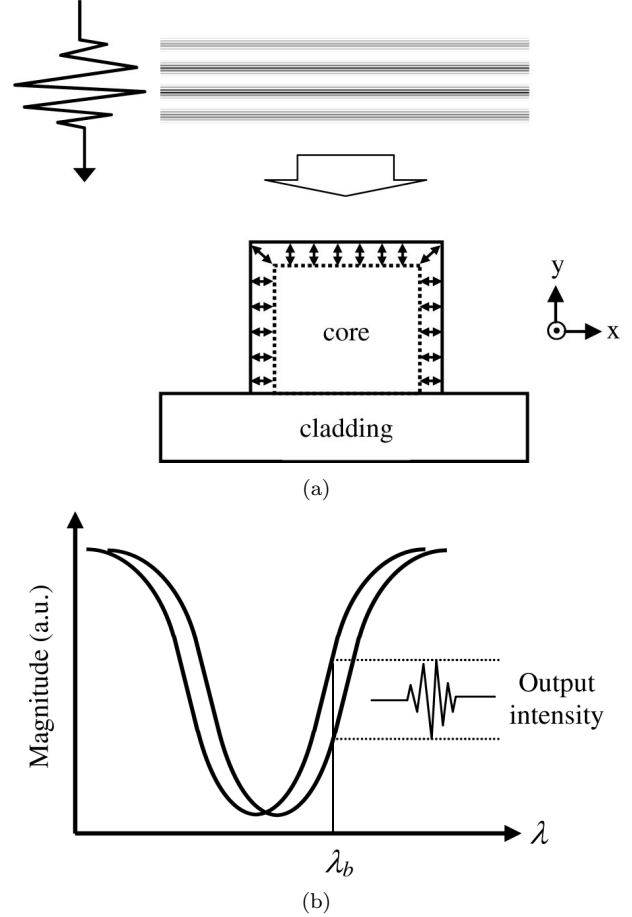


Fig. 2. (a) Schematic shows interaction between the waveguide and an incoming ultrasound pulse. The pulse stresses the structure, deforming the waveguide dimension and simultaneously modifying the refractive index of the core. To illustrate the concept clearly, the figure is not drawn to scale. Typically, the wavelength of the ultrasound wave is much larger than the waveguide dimension. (b) Ultrasound detection using the optical resonance of a microring sensor.

the effective refractive index of the guided mode, and in turn shift the resonance. With a fixed incident wavelength at  $\lambda_b$ , the output intensity, modulated by the ultrasound pulse through the optical resonance, is collected by a high-speed photodetector. Thus, the ultrasound signal is transduced into a detectable optical intensity signal, as shown in Fig. 2(b).

### B. Waveguide Deformation

For an acoustic wave propagating in water with frequency ranging from 10 to 50 MHz, the corresponding wavelength is between  $150 \mu\text{m}$  and  $30 \mu\text{m}$ . The optical waveguide height ( $< 2 \mu\text{m}$ ) is much smaller than the acoustic wavelength. Therefore, to calculate the elastic deformation of the waveguide due to acoustic pressure, a quasistatic approximation is used, in which the stress does not have shear components. The strain of an isotropic material can be related to the applied stress through [18]:

$$\begin{bmatrix} \varepsilon_x \\ \varepsilon_y \\ \varepsilon_z \end{bmatrix} = \frac{1}{E} \begin{bmatrix} 1 - \nu - \nu & & \\ -\nu & 1 - \nu & \\ -\nu & -\nu & 1 \end{bmatrix} \begin{bmatrix} \sigma_x \\ \sigma_y \\ \sigma_z \end{bmatrix}, \quad (5)$$

where  $\varepsilon_i$  and  $\sigma_i$  are the normal strain and stress in the  $i$  direction ( $i = x, y, \text{ or } z$ ), respectively.  $E$  represents the Young's modulus, and  $\nu$  is the Poisson's ratio of the material.

In the case of microring sensors,  $\sigma_x$  is equal to  $\sigma_y$ , and is denoted as  $-P$ . In addition, the strain along  $z$ , the direction of light propagation, is considered zero due to strong adhesion of the waveguide to the rigid substrate. With these boundary conditions, the strain components can be calculated as:

$$\varepsilon_x = \varepsilon_y = \frac{-(1+\nu)(1-2\nu)P}{E}. \quad (6)$$

and the stress along  $z$  as  $\sigma_z = -2\nu P$ . In our experiments, polystyrene microrings are used. Recent studies of mechanical properties of thin polymer films [19], [20] show significant softening for thin films compared with bulk polymers. A reduction of the Young's modulus by a factor of 10 from its bulk value for a 2- $\mu\text{m}$  thick polymer layer has been reported [20]. For a polystyrene thin film, the Young's modulus and the Poisson's ratio are  $0.3 \pm 0.1 \times 10^9$  Pa and 0.33, respectively [20]. With an applied acoustic wave having a magnitude of 1 MPa, the strain components of the waveguide,  $\varepsilon_x$  and  $\varepsilon_y$ , are equal to  $-1.5 \times 10^{-3}$  (i.e., -1.5 milistrain).

### C. Elasto-Optic Effect

Stress-induced strain also can change refractive index through the elasto-optic effect. Based on elasto-optic theory [21], the refractive indexes for  $x$ - and  $y$ -polarized light (coordinates shown in Fig. 2) can be expressed as:

$$\begin{aligned} n_x &\approx n_0 - C_1\sigma_x - C_2(\sigma_y + \sigma_z), \\ n_y &\approx n_0 - C_1\sigma_y - C_2(\sigma_z + \sigma_x), \end{aligned} \quad (7)$$

where  $n_0$  is the refractive index without stress ( $n_0 = 1.58$  at a wavelength of 1550 nm for polystyrene).  $C_1$  and  $C_2$  are elasto-optic constants. For a polystyrene thin film,  $C_1$  and  $C_2$  are  $48 \pm 3 \times 10^{-12}$  Pa $^{-1}$  and  $29 \pm 3 \times 10^{-12}$  Pa $^{-1}$  [20] at an optical wavelength of 632.8 nm. These values are used for estimation due to lack of experimental data measured in the infrared region, in which our experiments are performed. Again, with an applied acoustic wave with  $P = 1$  MPa, the indices,  $n_x$  and  $n_y$ , are increased by approximately  $1.0 \times 10^{-4}$ .

Applied stress also can change the refractive index of water. The empirical elasto-optic constant is  $1.5 \times 10^{-4}$  MPa $^{-1}$  [22]. Even though the elasto-optic constant of water has similar magnitude to that of polystyrene, the influence on the effective index is about 25 times smaller because the light field does not penetrate into the water significantly.

A positive strain field can shrink the waveguide dimension, leading to reduced  $n_{\text{eff}}$ . In contrast, the elasto-optic effect induced by the same strain increases the material index, enhancing  $n_{\text{eff}}$ . These two phenomena compete with each other. To understand which phenomenon dominates,

the effective index is estimated as a function of applied acoustic pressure accounting for both effects. The calculation is performed using the effective index method [23] on a polystyrene channel waveguide with a cross section of  $2.4 \mu\text{m} \times 1.85 \mu\text{m}$  sitting on silicon oxide. For both TE and TM polarizations, the effective index change is negative, which implies that waveguide deformation has a larger impact on  $n_{\text{eff}}$  than the elasto-optic effect. Assuming linearity in the stress-strain relations we find that the pressure dependence of  $n_{\text{eff}}$  is linear for levels below 1 MPa, with a slope of:

$$\frac{dn_{\text{eff}}}{dP} = -2.7 \times 10^{-5} \text{ MPa}^{-1}. \quad (8)$$

The shift in the resonant wavelength corresponding to the change in the effective refractive index can be evaluated using the resonance condition (4). The predicted wavelength shift is:

$$\frac{d\lambda_c}{dP} = \frac{\lambda_c}{n_{\text{eff}}} \frac{dn_{\text{eff}}}{dP} = -27 \text{ pm/MPa}. \quad (9)$$

### D. Sensitivity

The total sensitivity  $S$ , is defined as the change in the transmission coefficient due to a change in acoustic pressure. For a high Q-factor resonator, the transmission near the resonance has a sharp dependence on the one-pass phase shift  $\phi$ , which in turn depends on  $n_{\text{eff}}$ . Therefore, small changes in  $n_{\text{eff}}$  due to deformations of the waveguide are amplified leading to high sensitivity to acoustic pressure. Acoustic pressure also can deform the coupling region, leading to modifications in the coupling parameter  $\tau$ . The contribution of this effect to the total sensitivity is negligible, however, due to the slow dependence of the transmission on the coupling parameter. Therefore, the total sensitivity can be expressed as:

$$S(\lambda) = \frac{\partial T(\phi, a, \tau)}{\partial \phi} \frac{d\phi(\lambda)}{dn_{\text{eff}}} \frac{dn_{\text{eff}}}{dP} = \frac{2\pi L}{\lambda} \frac{\partial T}{\partial \phi} \frac{dn_{\text{eff}}}{dP}. \quad (10)$$

Assuming the operating point is near a resonance such that  $\phi \sim 2\pi m + \delta\phi$ , and using (1), the sensitivity can be expressed as a function of the microring parameters as:

$$S(\lambda) \approx \frac{2\pi L}{\lambda} \times \frac{2\tau a(1-\tau^2)(1-a^2)(\delta\phi)}{\left[(1-\tau a)^2 + 4\tau a \left(\frac{\delta\phi}{2}\right)^2\right]^2} \frac{dn_{\text{eff}}}{dP}. \quad (11)$$

The point of maximal sensitivity can be calculated from (8). This yields the phase-tuning value,  $\delta\phi_{\text{max}}$ , associated with the maximum sensitivity:

$$\delta\phi_{\text{max}} = \frac{1-\tau a}{\sqrt{3\tau a}}. \quad (12)$$

At this point, the total sensitivity and the absolute transmitted intensity become:

$$(S) \Big|_{\delta\phi=\delta\phi_{\text{max}}} \approx \frac{2\pi L}{\lambda} \times \frac{3\sqrt{3}}{8} \frac{\sqrt{\tau a}(1-\tau)(1-a)}{(1-\tau a)^3} \frac{dn_{\text{eff}}}{dP}, \quad (13)$$

and:

$$(I_t)|_{\delta\phi=\delta\phi_{\max}} \approx I_0 \times \frac{3}{4} \left[ \frac{1}{3} + \left( \frac{\tau - a}{1 - \tau a} \right)^2 \right]. \quad (14)$$

When the microring operates at the critical point at which the intensity coupled into the microring cavity is balanced with the loss inside the cavity (i.e.,  $\tau$  is equal to  $a$ ), zero transmission intensity can be achieved at resonance. Simultaneously, the transmission intensity with the maximum slope is  $(I_t)|_{\delta\phi=\delta\phi_{\max}} = I_0/4$ .

According to (10), the maximum slope depends on two parameters of the microring,  $\tau$  and  $a$ , with a fixed microring size and  $I_0$ . These parameters can be estimated by fitting the measured transmission spectrum to (1). Optimization of the sensitivity is gained by tuning these parameters through iterations in device design and fabrication. The amplitude self-coupling coefficient  $\tau$  can be controlled by adjusting the waveguide dimension, and the gap separation between the ring and straight waveguides. The amplitude attenuation factor  $a$ , is mainly affected by the radiation loss due to surface roughness and bending of the ring waveguide [24]. Surface roughness can be reduced by thermal reflow technique for polymer microrings[25]. Bending loss can be reduced by reducing the ring curvature or decreasing the operating wavelength.

### E. Maximum Modulation Frequency

The resonator has a finite optical bandwidth determined by the resonance width. It can be expressed as a function of the basic optical frequency  $\nu$  and the Q-factor:

$$\text{BW}_{\text{OPTIC}} = \frac{\nu}{Q}. \quad (15)$$

The finite optical bandwidth imposes an upper limit on detection bandwidth. For typical microring resonators, the resonant bandwidth ranges from 0.01 nm to several nm, leading to a bandwidth limit larger than 1 GHz.

Another factor influencing the maximum modulation frequency is the finite size of the microring structure. With the ultrasonic wavelength comparable to the waveguide dimension, a hydrostatic assumption is no longer valid. This reduces optical modulation in response to ultrasound. Acoustic reflections from the rigid substrate and the polymer-water boundary further reduce detection bandwidth. The extreme case occurs when the wavelength of ultrasound is equal to twice the waveguide height. For a polystyrene waveguide of  $2 \times 2 \mu\text{m}$  (taking into account the reduced Young's modulus of a thin film) this corresponds to a maximum modulation frequency of 200 MHz.

## III. FABRICATION

We chose polystyrene (PS) as the waveguide material to meet several design criteria. PS has relatively low Young's

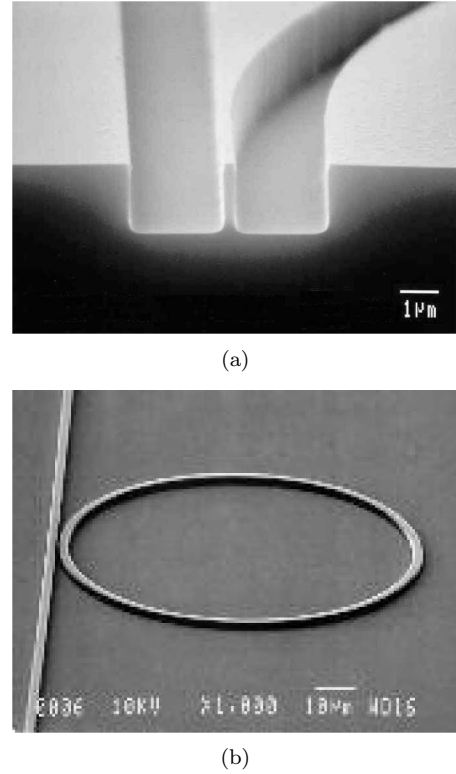


Fig. 3. (a) Cross section of a mold cleaved right at the coupling region. (b) An imprinted PS microring. Note the scale bars in each photograph.

modulus and, therefore, high deformation per unit pressure, leading to increased sensitivity. PS has low optical absorption throughout the visible and near IR range, enabling high Q-factor resonance to enhance sensitivity. In addition, polymers have other advantages, such as low cost and simple fabrication processes, which may lead to disposable sensor devices.

In our design, the waveguides are  $2.4 \mu\text{m}$  wide and  $1.85 \mu\text{m}$  high for single-mode operation at an optical wavelength of 1550 nm. The separation in the coupling region between the microring and straight waveguides is in the submicron regime, typically several hundred nanometers. To fabricate such high aspect-ratio polymer structures, a nanoimprint technique [26] is used due to its simple process, high fidelity, and precise dimension control. It starts from a mold with reverse patterns fabricated using electron-beam lithography, nanoimprint lithography, and reactive ion etching. The mold then is used to directly imprint a spin-coated polymer material on a substrate at appropriately elevated temperature and applied pressure. Heating makes the polymer easy to deform and flow, and the applied pressure squeezes and displaces the polymer to fill the trench patterns on the mold. The whole device structure then can be easily stamped. Detailed fabrication processes can be found in [27]. It can be applied to a variety of polymers, such as poly(methylmethacrylate), PS, and polycarbonate. Examples of a mold and an imprinted polystyrene microring are shown in Fig. 3.

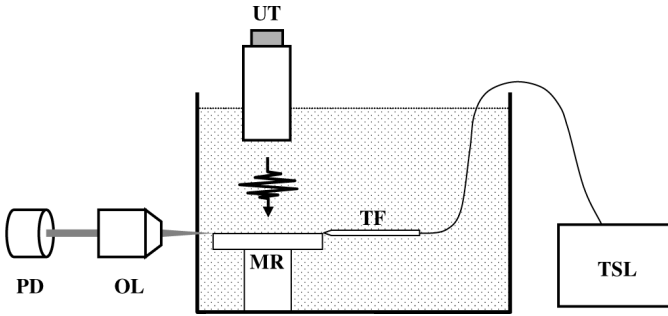


Fig. 4. Experimental setup used to test microring detection system. MR, microring sample; OL, objective lens; PD, photodetector; TF, tapered fiber; TSL, tunable semiconductor laser; and UT, ultrasound transducer.

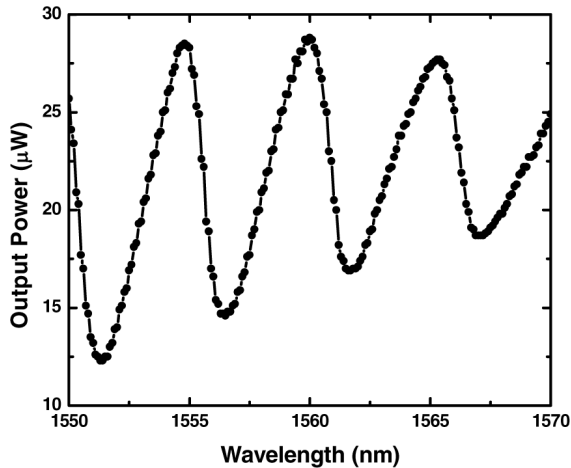


Fig. 5. Measured spectrum of the selected microring. The bias wavelength is chosen at 1550.5 nm.

#### IV. EXPERIMENTAL DEMONSTRATION OF SINGLE-MICRORING

The experimental setup shown in Fig. 4 is used to test the microring detection system. A microring sample is mounted inside a tank and immersed in water. Light from a tunable semiconductor laser (TSL-220, Santec, Hackensack, NJ) is coupled into the waveguide with a tapered fiber. Output light is collected by an objective lens and detected using a wide bandwidth amplified InGaAs photodiode (model 818-BB-30A, Newport, Irvine, CA). The PS microring has a diameter of  $95 \mu\text{m}$ . The microring spectrum first is measured, as shown in Fig. 5. The resonance has a fairly low Q-factor of about 600. From the spectrum, the incident wavelength is fixed at a bias wavelength of 1550.5 nm, at which the slope of resonance is maximal.

Ultrasound pulses, generated from a 50 MHz piezoelectric transducer [28] ( $\text{LiNbO}_3$ , aperture diameter 3 mm, focal length 4.5 mm, custom made by the Resource Center for Medical Ultrasonic Transducer Technology, University of Southern California, Los Angeles, CA) are applied to insonify the microring. The transducer, driven by a pulser/receiver (5910PR, Panametrics-NDT, Waltham, MA), is positioned such that ultrasound pulses are focused

on the sample surface. A pulse-echo measurement then is performed by receiving the reflection of the incident pulse back to the transducer. The received waveform is plotted in Fig. 6(a). Fig. 6(b) shows the optical output signal of the microring under the same modulation condition. The pulse arrival time of the optical signal is about one-half the round trip pulse-echo time. Frequency spectra of both waveforms can be calculated by fast Fourier transform, as shown in Fig. 6(c).

The pulse-echo exhibits a wide band of ultrasound signal ranging from 20 MHz to 65 MHz. The detected optical signal has similar spectral shape, except for a dip around 60 MHz. The reason for the dip is under investigation. The pulse-echo signal is shaped twice by the transducer response on both transmit and receive, whereas the optical signal from the microring is shaped only on transmit. This produces slightly different spectral shapes. The experimental result shows that the microring can respond to high-frequency ultrasound signals at least up to 55 MHz. From these two spectra, the frequency response of the microring detector can be obtained as illustrated in Fig. 7. The bandwidth is flat up to 25 MHz ( $-3 \text{ dB}$  bandwidth), except for a dip around 60 MHz. We believe that microrings should possess similarly flat response for low frequencies as well. Measured data are not accurate below 20 MHz due to the finite bandwidth of the ultrasound transducer.

To measure the sensitivity and noise equivalent pressure (NEP), a calibrated 10 MHz transducer (V311, 6.35 mm diameter, 19 mm focal length, Panametrics-NDT, Waltham, MA) is used. It generates a peak pressure of  $\sim 5 \text{ MPa}$ . A setup similar to Fig. 4 is used to measure the induced optical modulation signal. The spectral slope (Fig. 5) is used to convert the voltage signal of the photodetector to wavelength shift. The wavelength shift corresponding to an acoustic pressure of 5 MPa is 105 pm, leading to a sensitivity of 21 pm/MPa. This value is in close agreement with the expected value of 27 pm/MPa calculated using the theoretical model presented in Section II (9).

The measured sensitivity value is used to estimate the NEP to be 150 kPa with a 40 MHz bandwidth. This value is significantly higher than our previous result [13] because we used a resonator of lower Q-factor in the current experiment. The fabrication technology could enable increasing the Q-factor by more than an order of magnitude. Higher Q-factor increases the signal amplitude linearly, without elevating the noise level. Moreover, the sensitivity can be further improved by increasing the optical power coupled to the ring. In our current setup, an optical power of only  $20 \mu\text{W}$  is measured at the waveguide output. At least a 100-fold higher power can be obtained by increasing the laser output and improving the coupling efficiency. Under these conditions, the predicted NEP of the system would scale to a value of 15 KPa, representing performance almost two times better than a state-of-the-art PVDF hydrophone of similar size [29].

The active area of a single microring sensor was tested by scanning the focal spot of the ultrasonic transducer

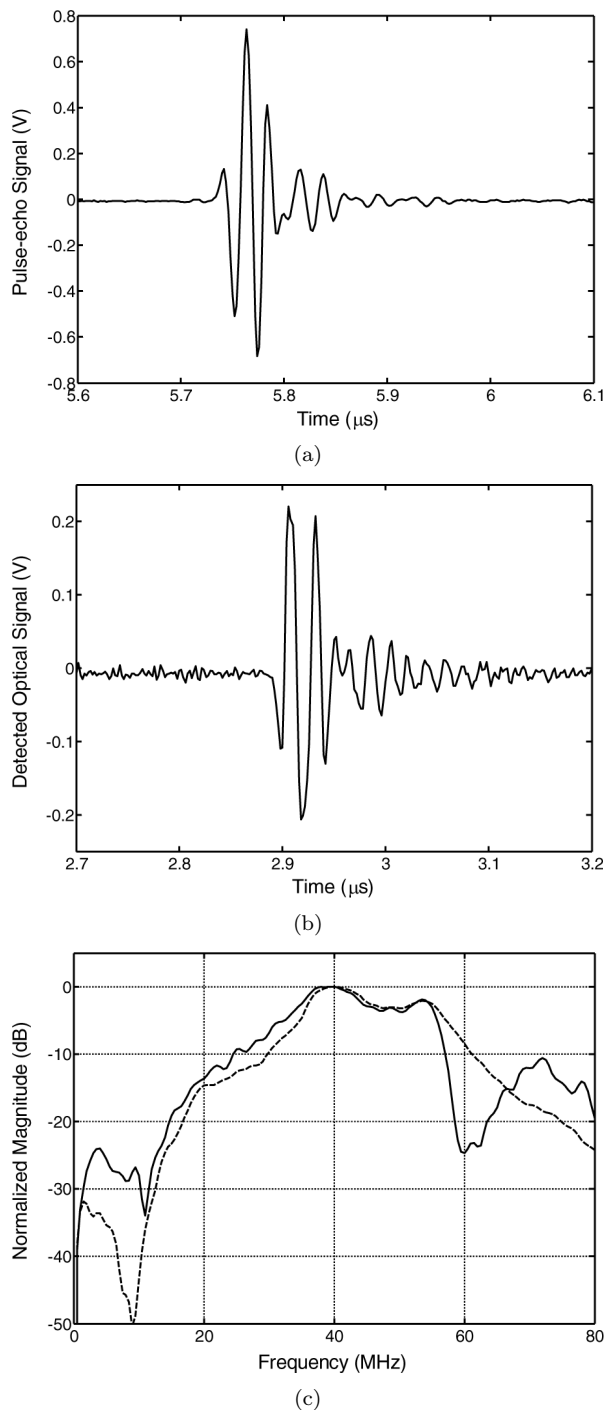


Fig. 6. (a) The received waveform reflected at the sample surface back to the transducer in a pulse-echo measurement. (b) The optical signal of the microring in response to an ultrasound pulse. (c) Normalized frequency spectra of the pulse echo (dashed line) and optical response of the microring (solid line).

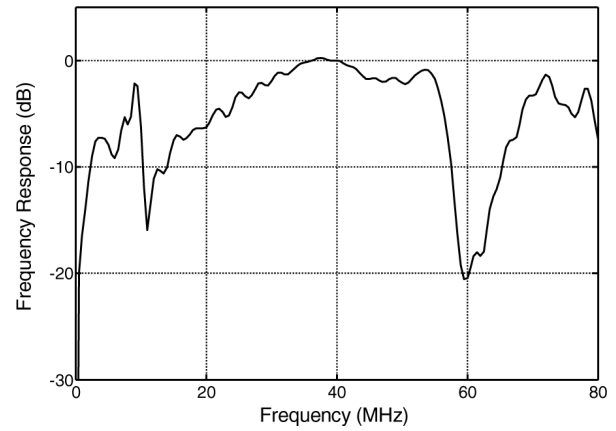


Fig. 7. Frequency response of a PS microring resonator to an ultrasound pulse.

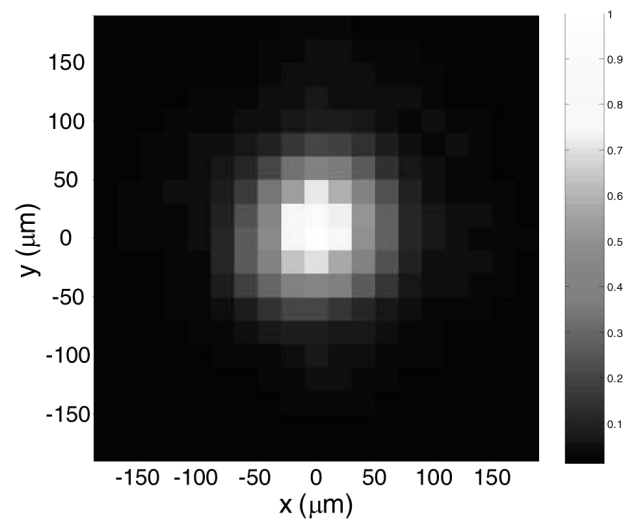


Fig. 8. 2-D scan of a focused pulse source over the microring: x axis is the direction along the straight waveguide, and y axis is parallel to the sample surface. The color bar represents linear scale of microring signal energy.

across the microring surface. The ultrasonic beam width (full width at half maximum) at the focal plane is estimated to be about  $80 \mu\text{m}$  at  $40 \text{ MHz}$  [30]. The scanning step then is chosen to be  $20 \mu\text{m}$ . The energy of the optical modulation signal for a two-dimensional (2-D) scan is plotted in Fig. 8. Nearly circular symmetry is demonstrated (consistent with the microring shape) and the full width at half maximum is about  $130 \mu\text{m}$ . A numerical calculation integrating the pressure field of the transducer along the microring circumference was performed. The induced optical signal was calculated by assuming a linear relation between the pressure and the effective refractive index. The calculation was performed for multiple positions of the transducer in order to simulate the experimental scan results. A ring diameter of  $90 \mu\text{m}$  was assumed. The simulation results are in close agreement with the measurement as shown in Fig. 9. Confinement of detection to the ring area demonstrates that multi-ring array operation is possible with minimal interelement cross talk.

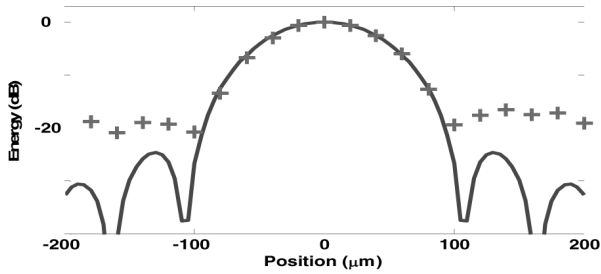


Fig. 9. Line scan of a focused 40 MHz transducer across the center of the microring. The measured optical signal (crosses) is in close agreement with calculation of pressure integral along the ring (line).

V. DESIGN OF HIGH-FREQUENCY OPTOACOUSTIC MICRORING ARRAYS

To use microring resonators in high-frequency ultrasound imaging, several design criteria must be fulfilled. In the high-frequency regime (20 MHz–50 MHz), the acoustic wavelength ranges from 75 μm to 30 μm. For a typical transducer array, the spacing between two adjacent elements is around the wavelength (typically  $0.5\lambda-0.8\lambda$ ). This implies that the radius of the microring should be less than 24 μm at 50 MHz and 60 μm at 20 MHz. Reduced ring radius might lead to loss of guiding capability in microring waveguides. For the example of PS microrings immersed in water, the index difference between the polymer core and the water media is too small to support light guiding at 1550 nm if the ring radius is less than 20 μm. This issue can be remedied by using shorter optical wavelengths or by using other materials with low Young’s modulus and high-refractive index.

For a polymer microring resonator, there are two main factors contributing to resonator loss: surface roughness scattering and bending loss [24], [25]. In most cases, the former dominates. Fortunately, this scattering loss can be greatly reduced in polymer microrings using thermal-reflow techniques [25], with which bending loss starts to dominate as ring size shrinks. Size shrinkage introduces more loss (reducing  $a$ ) to the resonator cavity and widens the resonance. This, in turn, lowers the resonant slope. To maintain large contrast between on- and off-resonance (i.e., to approach critical coupling),  $\tau$  should be decreased accordingly to provide sufficient light coupling into the microring.

Even though the resonant bandwidth of polymer microrings can be very narrow [31], leading to high sensitivity, it should be sufficiently wider than the resonant shift induced by ultrasound to avoid signal distortion.

To achieve the optimal design, the target frequency range should be chosen. Based on this range, the suitable microring size is determined to satisfy array requirements. From the microring size, the total loss or  $a$  can be estimated, then  $\tau$  is set by choosing a proper waveguide cross section and gap between microring and bus waveguides to optimize sensitivity.

Microring arrays can use multiplexing techniques developed for telecommunication applications, such as wave-

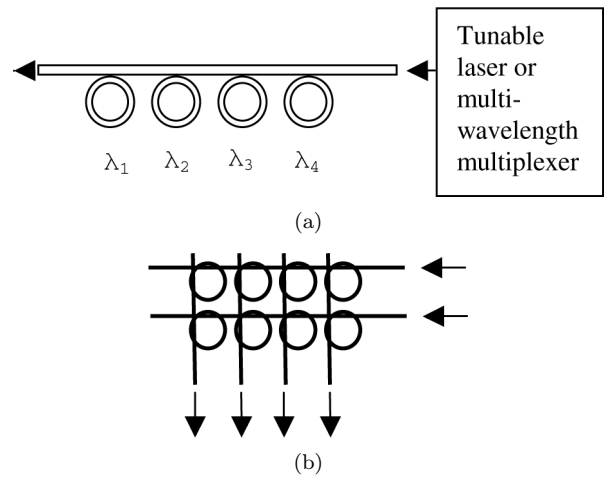


Fig. 10. (a) A linear array of microrings based on wavelength multiplexing and (b) 2-D array using multiple inputs and multiple outputs configuration.

length division multiplexing (WDM) [32], for element connectivity and addressing. Two examples of a potential microring array are shown schematically in Fig. 10. Fig. 10(a) shows a linear array formed by coupling all microrings to a common straight waveguide (signal bus). Each microring has slightly different diameter so that each element has different resonance frequency. A tunable laser can address each element at a time by wavelength selection, or a multiwavelength source can be used to probe all elements simultaneously.

In the second case, the transmitted optical signal at the bus output is first demultiplexed to route each optical wavelength signal into a separate photodetector. Fig. 10(b) shows a layout for a 2-D array that does not use frequency selection (all rings have the same resonance frequency). Instead, each microring acts as a transmission switch between horizontal and vertical waveguides. Any microring can be selected by choosing input and output waveguides. The two schemes also can be combined to have a 2-D array with wavelength selection along each row. This greatly minimizes the number of input/output lines required for addressing the array, making this scheme especially attractive for catheter-based, high-resolution, 3-D imaging applications, such as IVUS.

VI. CONCLUSIONS

Polymer microring resonators detecting high-frequency ultrasound signals were demonstrated. A simple theoretical model was introduced to describe interaction mechanisms between ultrasound and polymer waveguides. The model includes elastic deformation of the optical waveguide and refraction index modulation due to the elasto-optic effect. The model was used to predict the sensitivity and bandwidth of the microring detector.

A PS microring device has been fabricated using nano-imprint technique. The device was tested using 10 MHz

and 50 MHz ultrasonic transducers. We found good agreement between the measured sensitivity and the model predictions. By comparing pulse-echo signals with the microring optical modulation signal, the microring response was obtained. The bandwidth has a 10 dB rise from 15 MHz to 58 MHz and a dip around 60 MHz. In addition, a 2-D scan was performed to examine the effective detection area of a microring. Results illustrate that the effective area is close to the ring size, implying that array operation would be possible with minimal cross talk between elements. These features suggest potential application of polymer microring resonators in high-frequency ultrasound detection arrays. Several methods to realize microring detector arrays are suggested based on techniques used in optical routing applications for telecommunications.

#### ACKNOWLEDGMENT

We thank the Resource Center for Medical Ultrasonic Transducer Technology, University of Southern California, for providing us with high-frequency ultrasound transducers.

#### REFERENCES

- [1] J. E. Semmens and L. W. Kessler, "Non-destructive acoustic micro imaging (AMI) analysis of MEMS materials, manufacturing and packaging," *Proc. SPIE*, vol. 4558, pp. 260–267, Oct. 2001.
- [2] A. Liu, L. Joyner, and D. H. Turnbull, "Alteration of limb and brain patterning in early mouse embryos by ultrasound-guided injection of Shh-expressing cells," *Mech. Dev.*, vol. 75, pp. 107–115, July 1998.
- [3] S. Srinivasan, H. S. Baldwin, and O. Aristizabal, "Noninvasive, in utero imaging of mouse embryonic heart development with 40-MHz echocardiography," *Circulation*, vol. 98, pp. 912–918, Sep. 1998.
- [4] D. H. Turnbull, "In utero ultrasound backscatter microscopy of early stage mouse embryos," *Comput. Med. Imag. Graph.*, vol. 23, pp. 25–31, Jan./Feb. 1999.
- [5] D. H. Turnbull, J. A. Ramsay, G. S. Shivji, T. S. Bloomfield, L. From, D. N. Sauder, and F. S. Foster, "Ultrasound backscatter microscope analysis of mouse melanoma progression," *Ultrasound Med. Biol.*, vol. 22, no. 7, pp. 845–853, 1996.
- [6] D. E. Goertz, J. L. Yu, R. S. Kerbel, P. N. Burns, and F. S. Foster, "High-frequency Doppler ultrasound monitors the effects of antivasular therapy on tumor blood flow," *Cancer Res.*, vol. 62, pp. 6371–6375, Nov. 2002.
- [7] R. A. White, C. E. Donayre, G. E. Kopchok, I. Walot, C. M. Mehinger, E. P. Wilson, and C. de Virgilio, "Vascular imaging before, during and after endovascular repair," *World J. Surg.*, vol. 20, pp. 622–629, 1996.
- [8] M. Vogt, K. Kaspar, P. Altmeyer, K. Hoffmann, and S. El Gammal, "High frequency ultrasound for high resolution skin imaging," *Frequenz*, vol. 55, pp. 12–20, Jan./Feb. 2001.
- [9] P. J. Cao, W. H. Chen, N. Karkhanis, and K. K. Shung, "Accurate corneal thickness measurement using ultrasound," *Proc. SPIE*, vol. 4687, pp. 430–437, Apr. 2002.
- [10] J. C. Pavlin and S. F. Foster, *Ultrasound Biomicroscopy of the Eye*. New York: Springer-Verlag, 1995.
- [11] D. R. Holmes, III and R. A. Robb, "Trans-urethral ultrasound (TUUS) imaging for visualization and analysis of the prostate and associated tissues," *Proc. SPIE—Med. Imaging*, vol. 3976, pp. 22–27, Apr. 2000.
- [12] G. A. Rodriguez-Granillo, E. P. McFadden, J. Aoki, C. A. G. van Mieghem, E. Regar, N. Bruining, and P. W. Serruys, "In vivo variability in quantitative coronary ultrasound and tissue characterization measurement with mechanical and phased-array catheters," *Int. J. Cardiol. Imag.*, vol. 22, pp. 47–53, Feb. 2006.
- [13] S. Ashkenazi, C. Y. Chao, L. J. Guo, and M. O'Donnell, "Ultrasound detection using polymer microring optical resonator," *Appl. Phys. Lett.*, vol. 85, pp. 5418–5420, Nov. 2004.
- [14] J. D. Hamilton, T. Buma, M. Spisar, and M. O'Donnell, "High frequency optoacoustic arrays using etalon detection," *IEEE Trans. Ultrason., Ferroelect., Freq. Contr.*, vol. 46, pp. 160–169, Jan. 2000.
- [15] S. Ashkenazi, Y. Hou, T. Buma, and M. O'Donnell, "Optoacoustic imaging using thin polymer etalon," *Appl. Phys. Lett.*, vol. 86, art. no. 134102, pp. 1–3, Mar. 2005.
- [16] J. G. Laufer, P. C. Beard, and T. N. Mills, "Comparison of the photothermal sensitivity of an interferometric optical fiber probe with pulsed photothermal radiometry," *Rev. Sci. Instrum.*, vol. 73, pp. 3345–3352, Sep. 2002.
- [17] V. Wilkens, "Characterization of an optical multilayer hydrophone with constant frequency response in the range from 1 to 75 MHz," *J. Acoust. Soc. Amer.*, vol. 113, pp. 1431–1438, Mar. 2003.
- [18] R. C. Hibbeler, *Mechanics of Materials*. Upper Saddle River, NJ: Pearson Education, 2003, p. 513.
- [19] H.-C. Liou, R. Willecke, and P. S. Ho, "Study of out-of-plane elastic properties of PMDA-ODA and BPDA-PDA polyimide thin films," *Thin Solid Films*, vol. 323, pp. 203–208, June 1998.
- [20] F. Ay, A. Kocabas, C. Kocabas, and A. Aydinli, "Prism coupling technique investigation of elasto-optical properties of thin polymer films," *J. Appl. Phys.*, vol. 96, pp. 7147–7153, Dec. 2004.
- [21] K. Okamoto, *Fundamentals of Optical Waveguides*. San Diego, CA: Academic, 2000, p. 265.
- [22] J. E. Parsons, C. A. Cain, and J. B. Fowlkes, "Cost-effective assembly of a basic fiber-optic hydrophone for measurement of high-amplitude therapeutic ultrasound fields," *J. Acoust. Soc. Amer.*, vol. 119, pp. 1432–1440, Mar. 2006.
- [23] H. Nishihara, M. Haruna, and T. Suhara, *Optical Integrated Circuits*. New York: McGraw-Hill, 1989, pp. 31–32.
- [24] V. Van, P. P. Absil, J. V. Hryniewicz, and P.-T. Ho, "Propagation loss in single-mode GaAs-AlGaAs microring resonators: Measurement and model," *J. Lightwave Technol.*, vol. 19, pp. 1734–1739, Nov. 2001.
- [25] C. Y. Chao and L. J. Guo, "Reduction of surface scattering loss in polymer microrings using thermal-reflow technique," *IEEE Photon. Technol. Lett.*, vol. 16, pp. 1498–1500, June 2004.
- [26] S. Y. Chou, P. R. Krauss, W. Zhang, L. Guo, and L. Zhuang, "Sub-10 nm imprint lithography and applications," *J. Vac. Sci. Technol. B*, vol. 15, pp. 2897–2904, Nov./Dec. 1997.
- [27] C.-Y. Chao and L. J. Guo, "Polymer microring resonators fabricated by nanoimprint technique," *J. Vac. Sci. Technol. B*, vol. 20, pp. 2862–2866, Nov./Dec. 2002.
- [28] J. Cannata, T. Ritter, W. H. Chen, R. H. Silverman, and K. K. Shung, "Design of efficient broadband single element (20–80 MHz) ultrasonic transducers for medical imaging applications," *IEEE Trans. Ultrason., Ferroelect., Freq. Contr.*, vol. 50, pp. 1548–1557, Nov. 2003.
- [29] P. C. Beard, H. Hurrell, E. van den Elzen, and T. N. Mills, "Comparison of a miniature, ultrasonic, optical fiber hydrophone with PVDF hydrophone technology," in *Proc. IEEE Ultrason. Symp.*, 1998, p. 1881, Oct. 1998.
- [30] X. Chen, K. Q. Schwarz, and K. J. Parker, "Radiation pattern of a focused transducer: A numerically convergent solution," *J. Acoust. Soc. Amer.*, vol. 94, pp. 2979–2991, Nov. 1993.
- [31] C. Y. Chao, W. Fung, and L. J. Guo, "Polymer microring resonators for biochemical sensing applications," *IEEE J. Select. Topics Quantum Electron.*, vol. 12, pp. 134–142, Jan./Feb. 2006.
- [32] S. J. Choi, Z. Peng, Q. Yang, S. J. Choi, and P. D. Dapkus, "An eight-channel demultiplexing switch array using vertically coupled active semiconductor microdisk resonators," *IEEE Photon. Technol. Lett.*, vol. 16, pp. 2517–2519, Nov. 2004.



**Chung-Yen Chao** was born in Taipei, Taiwan, R.O.C. in 1973. He received the B.S. degree in electrical engineering and the M.S. degree in electro-optical engineering from the National Taiwan University, Taipei, Taiwan, R.O.C., in 1995 and 1997, respectively, and the Ph.D. degree in electrical engineering from the University of Michigan, Ann Arbor in 2004. He recently completed his postdoctoral research at the University of Michigan.

His research interests include nanofabrication technology, design and fabrication of integrated optical devices in the applications of telecommunication, bio-chemical sensing, and medical diagnoses.



**Shai Ashkenazi** (M'00) received the B.Sc. degree in physics from the Technion Israel Institute of Technology, Haifa, Israel, in 1988, and his Ph.D. degree in physics from the Weizmann Institute of Science, Rehovot, Israel, in 1997. He then worked for 6 years in research and development companies in the fields of ultrasonic and optical devices for medical applications. In 2003, he moved to the University of Michigan, Ann Arbor, MI, where he is currently a research scientist.

His research interests include medical imaging and nanotechnology.



**Sheng-Wen Huang** was born in 1971 in Changhua, Taiwan, R.O.C. He received the B.S. and Ph.D. degrees from National Taiwan University, Taipei, Taiwan, R.O.C., in 1993 and 2004, respectively, both in electrical engineering. He worked as a postdoctoral researcher at National Taiwan University from 2004 to 2005, and is currently a postdoctoral researcher with the Department of Biomedical Engineering at the University of Michigan, Ann Arbor, MI.

His current research interests include thermal strain imaging, coded excitation, and optoacoustic transduction and imaging.



**Matthew O'Donnell** (M'79–SM'84–F'93) received the B.S. and Ph.D. degrees in physics from the University of Notre Dame, Notre Dame, IN, in 1972 and 1976, respectively. Following his graduate work, Dr. O'Donnell moved to Washington University in St. Louis, MO, as a postdoctoral fellow in the Physics Department working on applications of ultrasonics to medicine and nondestructive testing. He subsequently held a joint appointment as a senior research associate in the Physics Department and a research instructor of medicine in the Department of Medicine at Washington University.

In 1980 he moved to General Electric Corporate Research and Development Center in Schenectady, NY, where he continued to work on medical electronics, including MRI and ultrasound imaging systems. During the 1984–1985 academic year, he was a visiting fellow in the Department of Electrical Engineering at Yale University in New Haven, CT, investigating automated image analysis systems. In a bold move during 1990, Dr. O'Donnell became a professor of electrical engineering and computer science at the University of Michigan in Ann Arbor, MI. Since 1997, he has held a joint appointment as Professor of Biomedical Engineering at Michigan, and in 1998 he was named the Jerry W. and Carol L. Levin Professor of Engineering. Currently, he is the Chair of the Biomedical Engineering Department.

His most recent work has explored new imaging modalities in biomedicine, including elasticity imaging, in-vivo microscopy, optoacoustic arrays, optoacoustic contrast agents for molecular imaging and therapy, thermal strain imaging, and catheter-based devices.



**L. Jay Guo** (S'96–M'97) received his Ph.D. degree from the University of Minnesota, Minneapolis, MN, in 1997.

He was a Research Associate at Princeton University, Princeton, NJ, from 1998 to 1999. He is currently an associate professor in the Department of Electrical Engineering and Computer Science, University of Michigan, Ann Arbor, MI.

His research areas include organic electronics, nanoimprinting, nanophotonics, nanofabrication technologies with applications in polymer photonic devices and biotechnologies.